

# Real-time tracking the energy flow in cluster formation

Michael Stadlhofer,\* Bernhard Thaler,\* Pascal Heim,\* Josef Tiggesbäumker,† and Markus Koch‡  
(Dated: December 3, 2024)

While photodissociation of molecular systems has been extensively studied over decades, the photoinduced formation of chemical bonds remains largely unexplored. Especially for larger aggregates, the electronic and nuclear dynamics involved in the cluster formation process remain elusive. This limitation is rooted in difficulties to prepare reactants at well-defined initial conditions. Here, we show that this hurdle can be overcome by exploiting the exceptional solvation properties of superfluid helium nanodroplets ( $\text{He}_N$ ). We load the droplets with magnesium (Mg) atoms and investigate the dynamical response of the formed  $\text{Mg}_n$  aggregates to photoexcitation with femtosecond time-resolved photoelectron spectroscopy. Beside the response expected for conventional  $\text{Mg}_n$  clusters, consisting of a prompt signal rise and a decay characteristic for van der Waals bonds, the transient spectra also show a delayed photoelectron band peaking at 1.2 ps. This delayed signal rise is characteristic for nuclear dynamics and represents the photoinduced transition of  $\text{Mg}_n$  aggregates from a metastable, foam-like configuration, where Mg atoms are stabilized with a previously predicted interatomic spacing of 9.5 Å, to a compact cluster. With global fitting analysis and photoion-photoelectron coincidence detection, the concerted electronic and nuclear dynamics can be tracked on a fs timescale. We find that cluster formation, proceeding with a characteristic time constant of  $(450 \pm 180)$  fs, is accompanied by the population of highly-excited atomic states, exceeding the photoexcited state by up to 3 eV. We propose an energy pooling reaction in collisions of two or more excited Mg atoms during cluster formation as the mechanism leading to population of these high-lying Mg states. Additionally, conversion to kinetic energy through relaxation of the highly-excited states leads to fragmentation and enables ionic cluster fragments to overcome the He droplet solvation energy. These results underline the potential of  $\text{He}_N$  for time-resolved studies of bond formation and to uncover involved processes, such as photon energy upconversion.

## I. INTRODUCTION

Chemical reactions essentially consist of breaking and forming of molecular bonds. The mechanistic understanding of photoinduced bond breaking has been particularly shaped through femtosecond pump-probe spectroscopy. [1–3] Real-time tracking of the electronic and nuclear structure has provided insight into various processes accompanying photodissociation, such as curve crossings [4, 5], predissociation [6] conical intersections [7], or electronic relaxation [8].

Photoassociation is used to form molecules in ultracold atomic clouds [9, 10], where the binding energy is dissipated into the light field [11]. In the time-domain, however, photoassociation has largely escaped observation so far, in particular for larger systems, due to difficulties in preparing the reactants in a well-defined initial geometry. This limitation could be overcome only in a few situations: In gas phase, where the broad distribution of impact parameters completely blurs the time resolution, bond formation could only be observed for selected dimer molecules through Franck-Condon filtering based on the resonance condition for laser excitation [12–14]. In a few

cases, cold bimolecular van der Waals complexes [15–18], and anionic clusters [19], provide favorable initial conditions to study bond formation. In solution, a network of species separated by well-defined distances are readily achieved, however, inhomogeneous broadening prevents observation of individual states and structural dynamics can only be inferred by x-ray scattering [20, 21]. Despite these versatile approaches, the formation of clusters larger than dimer molecules and bimolecular aggregates has not been experimentally realized so far.

The endeavor to combine the advantages of the previous approaches—homogeneous distances in solution, low environmental perturbation for well-defined resonances, and low temperatures in gas phase—leads us to the application of helium nanodroplets ( $\text{He}_N$ ) as a cryogenic solvent. Helium nanodroplets have routinely been used for the synthesis and investigation of atomic and molecular aggregates, since they provide a high degree of control in the aggregation process, efficient cooling to 0.37 K, and enable measurements with low matrix effects compared to other noble gas environments [23–26]. Here, we show that the unique solvation properties of superfluid He can be used to prepare well-defined initial conditions for the time-resolved observation of bond formation of multiple reactants. This demonstration builds on recent observations that atoms solvated in  $\text{He}_N$  can arrange in metastable configurations at nanometer distance, enabled by the ultracold He solvent [27–33]. For two Mg atoms inside a  $\text{He}_N$ , density functional theory simulations predict such a metastable configuration at 9.5 Å interatomic distance, instead of the formation of a  $\text{Mg}_2$  molecule [34]. This dilute configuration is enabled

---

\* Institute of Experimental Physics, Graz University of Technology, Petersgasse 16, 8010 Graz, Austria.

† Institute of Physics, University of Rostock, 18059 Rostock, Germany; Department of Life, Light and Matter, University of Rostock, 18059 Rostock, Germany

‡ Institute of Experimental Physics, Graz University of Technology, Petersgasse 16, 8010 Graz, Austria.; markus.koch@tugraz.at

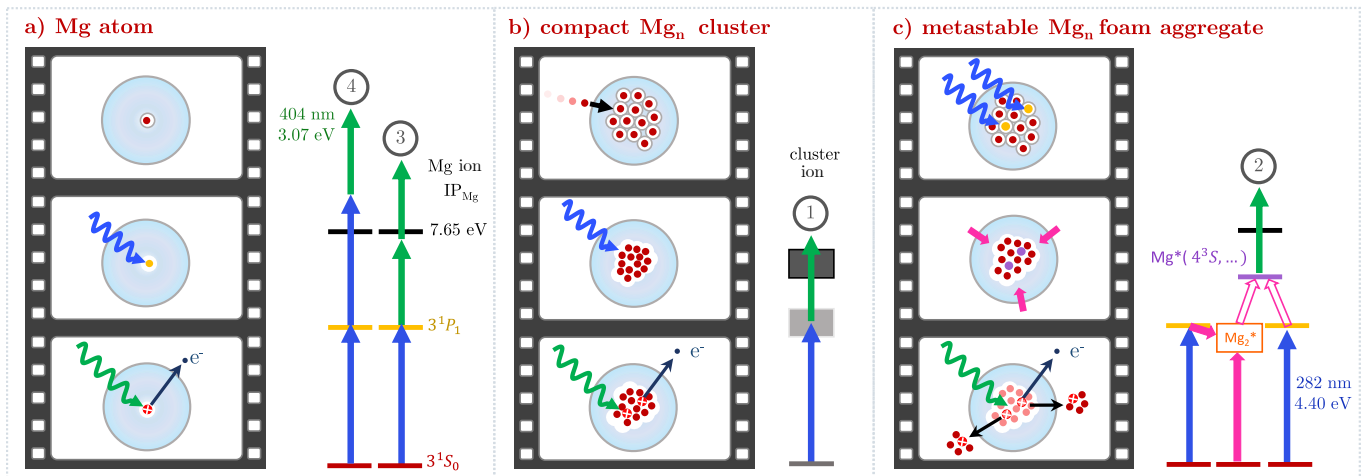


FIG. 1. Sketch of the photoinduced dynamics of single Mg atoms, compact  $\text{Mg}_n$  cluster and metastable  $\text{Mg}_n$  foam inside  $\text{He}_N$ . The corresponding energy level diagrams depict pump (blue)–probe (green) photoionization and different ionization pathways are labelled with (1) to (4), correspondingly to the photoelectron bands in Fig. 2. (a) Three-photon ionization channels of Mg atoms. (b) Formation of compact  $\text{Mg}_n$  cluster through collision of an energetic Mg atom with the foam-like aggregate during the pickup process [22] and subsequent pump–probe photoionization. (c) Photoexcitation of Mg atoms within the  $\text{Mg}_n$  foam triggers the transition to a compact cluster. Energy pooling (magenta arrows) leads to population of highly excited Mg levels [band (2)] and fragmentation.

through the accumulation of helium density between two Mg atoms, and referred to as “foam” [34] or “quantum gel” [35, 36]. We note that this prediction has been subject to discussion, since path integral Monte Carlo simulations of two and three Mg atoms inside  $\text{He}_N$  find no evidence for stabilization in a metastable configuration, but only equilibration to the strongly bound dimer and trimer [37].

Here, we present an investigation of the dynamical response of  $\text{Mg}_n$  aggregates inside  $\text{He}_N$  to photoexcitation with femtosecond photoelectron and -ion spectroscopy. [2, 3]. This approach has recently proven successful inside  $\text{He}_N$  for the observation of electronic [38, 39] and nuclear dynamics [40, 41]. We obtain time-resolved photoelectron spectra (TRPES) containing two different dynamic signatures, indicating that  $\text{Mg}_n$  aggregates exist in two different configurations inside  $\text{He}_N$ . An immediate signal rise followed by a fast  $\tau_1 = (380 \pm 70)$  fs decay is characteristic for van der Waals cluster, where primary processes are electronic dynamics (Fig. 1 b). In addition to this swiftly responding compact cluster, the TRPES also contains a PE band with delayed signal rise peaking 1.2 ps after photoexcitation and a much slower  $\tau_2 = (4.0 \pm 0.9)$  ps decay. We interpret this slower response to photoexcitation as a signature for nuclear dynamics involved in the transition leading from the predicted foam-like  $\text{Mg}_n$  configuration to a dense cluster (Fig. 1c). This transient signal reveals insight into the energy flow and nuclear dynamics during cluster formation.

## II. EXPERIMENT

Following a previous approach [38], helium nanodroplets with a mean radius of 5.3 nm (13500 He atoms per droplet) are loaded with about ten Mg atoms (see Supplemental VII A for further details). Using an amplified Ti:sapphire laser (800 nm center wave length, 25 fs pulse duration), short pulses are generated and split into a pump and probe arm. The cross-correlation signal of the pump and probe pulse has a duration of  $(45 \pm 3)$  fs. The pump pulse is tuned to 282 nm (4.40 eV photon energy) by an optical parametric amplifier, in order to trigger the collapse of the foam-like  $\text{Mg}_n$  aggregate through  $\text{Mg } 3^1P_1 \leftarrow 3^1S_0$  excitation, which appears slightly blue-shifted in the aggregate [33] relative to the bare atom transition [42] (see Fig. 1a). The probe pulse at 404 nm (3.07 eV), obtained through frequency doubling, ionizes the system and photoelectron spectra are recorded with a magnetic bottle time-of-flight spectrometer. The time-resolved variation of these photoelectron spectra, recorded through variation of the pump–probe time delay, provides insight into the evolution of excited state populations. Applying a high voltage pulse to the repeller electrode about 100 ns after the laser pulses accelerates the remaining ions towards the detector and thus allows for a simultaneous detection of electrons and ions in each laser shot [43]. This procedure enables a statistical analysis of covariances between electron energy and ion species. [44–46].

### III. RESULTS

The time-resolved photoelectron spectrum is shown in Fig. 2, depicted as a function of the electron binding energy. We first allocate the observed photoelectron bands to pump-probe ionization pathways based on energetic considerations. The temporal development of these bands, obtained from a global fitting analysis, reveals population transfers dynamics triggered by photoexcitation. Examination of the time-resolved ion yields and, in particular, the correlation of ion fragments to the photoelectron bands gives information about the accompanying nuclear dynamics.

**Assignment of photoelectron bands.** Inspection of Fig. 2a reveals four distinct bands. Band (1) between 2 and 3 eV rises instantaneously and shows a fast decay (Fig. 2b, yellow circles). Band (2) between 1 and 2 eV shows initially a cross correlation feature, followed by a moderate signal rise peaking at 1.2 ps and a slower decay than band (1) (Fig. 2b, purple circles). The assignment of bands (1) and (2) in Fig. 2 is difficult due to their overlap in time and energy. Both bands are related to states with binding energies lower than that of the photoexcited bare-atom  $3^1P_1$  state (3.30 eV binding energy), given the lower probe photon energy of only 3.07 eV. Bands (3) and (4) can be assigned to two-photon ionization of the excited  $3^1P_1$  Mg state (see Fig. 1a). Band (3) extends from 0.17 eV to -0.5 eV with a fast rise and slower decay, followed by a second slow rise after 10 ps (see Fig. 2b). This band represents the transient population of  $3^1P_1$  Mg state, ionized by two probe photons. The brief appearance of band (4) around  $t_0$  is characteristic for a cross-correlation peak: With a binding energy slightly below -1 eV we assign this band to  $3^1P_1$  ionization with one pump and one probe photon.

TABLE I. Relevant parameters of the three decay functions as obtained from the global fitting procedure (see Appendix VII B for formulas of the decay functions). Uncertainties represent a confidence level of 95%. In addition to the parameter and its value, the rightmost column indicates the DAS corresponding to the decay function.

parameter	value / fs	feature
time zero, $t_0$	$45 \pm 4$	all
temporal instrument response, $\sigma$	$170 \pm 15$	all
$N_1$ decay time, $\tau_1$	$380 \pm 70$	DAS <sub>1</sub>
$N_2$ rise time, $\tau_2^{rise}$	$450 \pm 180$	DAS <sub>2</sub>
$N_2$ decay time, $\tau_2$	$4000 \pm 900$	DAS <sub>2</sub>
$N_3$ decay time, $\tau_3$	$1090 \pm 90$	DAS <sub>3</sub>

**Global fitting analysis to retrieve population transfer dynamics.** The spectral and temporal over-

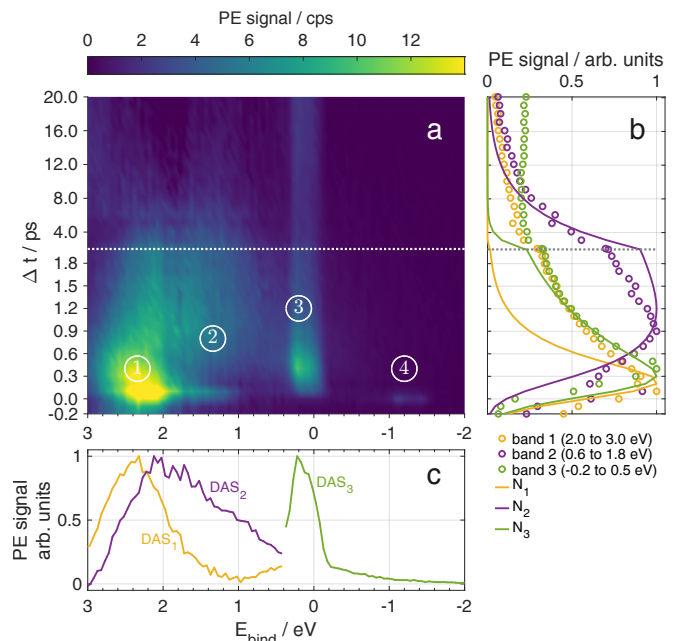


FIG. 2. Time-resolved photoelectron spectrum of  $Mg_n$  aggregates embedded in  $He_N$  and global fitting analysis. Note that below 2 ps, the spectra feature a higher temporal resolution. (a) Pseudocolor plot showing the transient electron yield as function of binding energy. Four distinct bands are marked (1) to (4). (b) Comparison of energy-integrated PE transients (see legend) to decay functions  $N_{1,2,3}$  from global fitting. (c) Decay associated spectra DAS<sub>1,2,3</sub> obtained from global fitting.

lap of bands (1) and (2) in the time-resolved photoelectron spectrum (Fig. 2) poses a challenge for a quantitative analysis. In order to decode the different contributions, the spectrum is analyzed by applying a global fitting procedure [47, 48], i.e., species with different transient behavior contributing to the spectrum are identified by extracting the respective decay associated spectra, DAS( $E$ ), and the associated transient decay functions,  $N(t)$ . Since the photoelectron bands in Fig. 2 differ in their signal rise behavior, we use two different types of decay functions: An instantaneous signal rise is modeled by a directly excited state followed by population decay (a Gaussian function convoluted with an exponential decay, as described in detail in Appendix VII B). A delayed signal rise is modeled by assuming sequential population transfer from an initially excited state (which is not necessarily detected) into the state yielding the photoelectron signal of the observed band. This function accounts for an exponential signal rise followed by an exponential decay, with two different characteristic time constants. Taking into account photoelectron-band assignments already made, one can simplify the fit process: Since band (3) originates from a different ionization process than bands (1) and (2) and since there is no overlap of band (3) with bands (1) and (2), one can split the time-resolved PE data into two energy domains at 0.42 eV

binding energy. The low binding energy region, containing the  $3^1P_1$  atom band (3), is modeled by DAS<sub>3</sub> (Fig. 2c, green line). The  $3^1P_1$  population appears instantly (Fig. 2b, green line), suggesting direct excitation by the pump pulse, and then decays with a time constant of  $\tau_3 = (1.1 \pm 0.1)$  ps.

Relevant parameters of the decay functions are listed in Tab. I for better comparability. From this transient signal, one can deduce the temporal pump-probe overlap (time zero,  $t_0$ ) and the temporal instrument response function duration  $\sigma$ . Inspection of the low binding energy region in Fig. 2 shows that the signal rises towards long delay times, which is not represented by the fit function. We account for this deviation by introducing an additional background, as described in Appendix VII B. Furthermore, the pump-probe cross correlation signal of band (4) is determined to be  $(45 \pm 3)$  fs in a separate measurement of the total electron yield around time zero. This cross correlation signal, together with  $t_0$  and  $\sigma$ , is kept constant in the remaining global fitting process.

In the high binding-energy domain two distinct populations, represented by different decay associated spectra and different decay functions, can be expected. In agreement with this assumption, DAS<sub>1</sub> with a peak at 2.5 eV (Fig. 2c, yellow line) and the broader DAS<sub>2</sub> peaking at 2 eV (purple line) can be identified, together with two corresponding decay functions. The transient population  $N_1$  rises quickly to a maximum at  $\sim 250$  fs, followed by a rapid decay with a characteristic time of  $\tau_1 = (380 \pm 70)$  fs (Fig. 2b, yellow line).  $N_2$  features a delayed onset with respect to  $N_1$  with a rise time of  $\tau_2^{\text{rise}} = (450 \pm 180)$  fs leading to a maximum at 1.2 ps and also a slower decay time constant of  $\tau_2 = (4.0 \pm 0.9)$  ps (Fig. 2b, purple line).

**Interpretation of DAS populations.** The different transient behavior of bands (1) and (2) indicates that they represent two different species. The sudden appearance of band (1) represents direct electronic excitation, presumably of compact  $Mg_n$  clusters. These compact clusters have a reduced electron binding energy compared to Mg atoms [22] and can thus be ionized by the probe pulse immediately after excitation (see Fig. 1b). The picosecond delay in the onset of band (2), in contrast, suggests that nuclear dynamics are involved, which are caused by the population of an undetected excited state. A possible origin would be the presence of a previously suggested foam-like  $Mg_n$  configuration, in combination with a transition to a compact  $Mg_n$  cluster triggered through  $3^1P_1 \leftarrow 3^1S_0$  photoexcitation by the pump pulse (see Fig. 1b). [31, 33, 34] Given the  $3^1P_1$  excited state binding energy of 3.30 eV, it is remarkable that DAS<sub>2</sub> indicates transient population within the whole detection window given by the 3.07 eV photon energy of the probe pulse. In this scenario, the occupation of these highly excited states is caused by the transition of  $Mg_n$  aggregates from a dilute to a compact configuration.

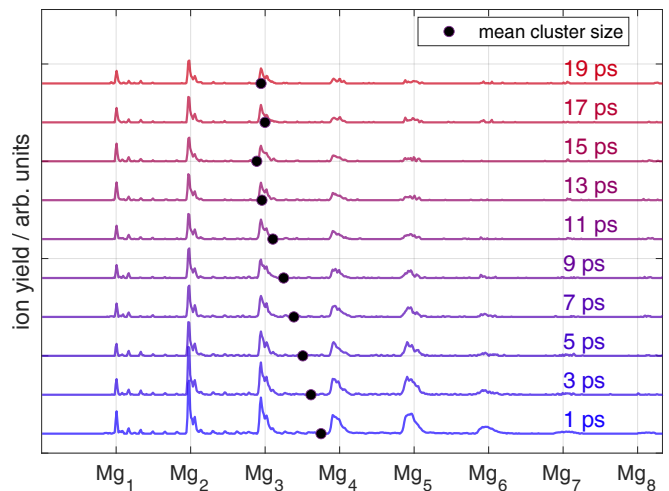


FIG. 3. Ion mass spectra for different pump-probe time delays, representing the transient fragment distribution of  $Mg_n^+$  cluster ions formed after photoexcitation and probe ionization. The spectra are area normalized and vertically offset according to the time-delay, indicated for each spectrum on the right side. Both isolated  $Mg_n^+$  cluster and  $Mg_n^+$ -He<sub>m</sub> snowballs are present in the mass spectra. The spectra were obtained by averaging the ion mass spectra in 2 ps time intervals and the mean cluster size is indicated as a black dot.

Testing the hypothetical assignment of band (1) to a compact  $Mg_n$  cluster and band (2) to a forming  $Mg_n$  cluster, the dependence of the photoelectron signal on the Mg doping level (see Supplemental Fig. 6) was investigated. At high doping, band (2) decreases and band (1) increases in relative strength, consistent with earlier studies of the spontaneous collapse of the dilute Mg aggregate at high Mg doping concentrations [22].

Direct photoexcitation of Mg atoms to states with such low binding energy, as an alternative explanation for the observed high binding energies, can be excluded since two-photon excitation leads to ionization (4.4 eV photon energy, 7.65 eV ionization energy [42]). Also, combined excitation with one pump and one probe photon can be excluded since this can only occur when pump and probe pulse overlap.

**Transient photoion signal.** A more direct insight into the nuclear dynamics and in particular the fragmentation behavior can be gained from the ion signals. Ions expelled from the droplet show up at optical delays larger than  $\Delta t \geq 1$  ps. Figure 3 shows pump-probe ion spectra recorded at selected time-delays. The spectra consist of peaks corresponding to  $Mg_n^+$  ( $n = 1 - 8$ ) cluster and  $Mg_n^+$ He<sub>m</sub> snowballs.

The pump-probe spectra show ion signals only up to  $Mg_8^+$ , while in the probe-only signal, masses as high as  $Mg_{12}^+$  appear. The average cluster size, taken as a measure and indicated by a black dot in Fig. 3 for each spectrum, decreases from 3.7 to 2.8 with increasing delay. Neglecting that the ionization probability may

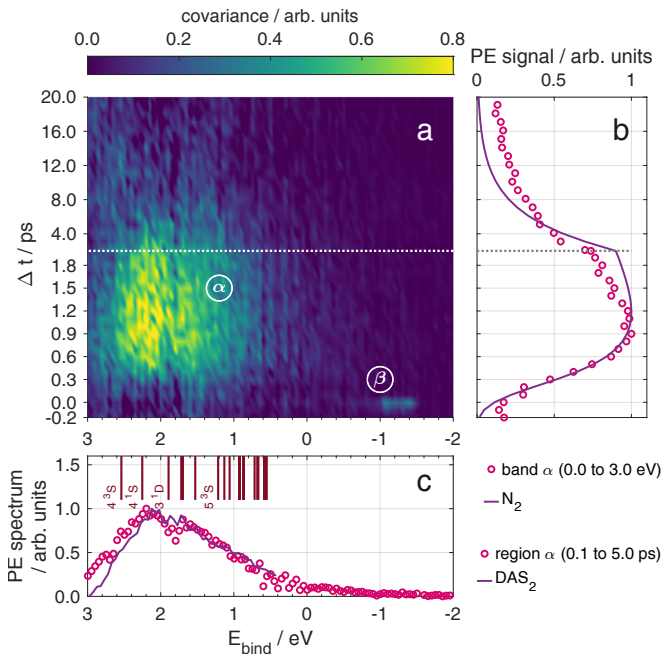


FIG. 4. Time-resolved photoelectron-photoion covariance spectrum of  $\text{Mg}_n$  aggregates inside  $\text{He}_N$ . (a) Pseudocolor plot of TRPES correlated to ion masses between 16 and 300 u. Two energy bands ( $\alpha$ ) and ( $\beta$ ) are marked. (b) Comparison of energy-integrated covariance band ( $\alpha$ ) to the time-dependent decay function  $N_2$  of  $\text{DAS}_2$ . (c) Comparison of the time-integrated covariance band ( $\alpha$ ) to  $\text{DAS}_2$ . Red vertical lines indicate highly excited Mg atom states.[42]

change with cluster size, this down-shift reflects the general trend that an increasing amount of energy is transferred to nuclear degrees of freedom with time.

#### Correlated electron-ion detection to identify fragmentation dynamics.

To further test the assignment of TRPES band (1) to compact  $\text{Mg}_n$  cluster and band (2) to foam-like aggregates, we examine correlations between photoelectrons and ions through covariance detection. [44–46] The assignment of ion fragments to each of the bands is of particular interest. This detection method has been applied to gas-phase molecules, where it allows to distinguish between different photochemical reaction pathways based on the ionic products [49–51]. For photoionization inside a helium droplet, the electrostrictive attraction prevents ion detachment from the droplet, except for situations where the ions gain sufficient kinetic energy through photodissociation [52, 53], or Coulomb explosion [41, 54]. In our case, we will see that the processes behind photoelectron band (1) and (2) differ significantly in the probability to yield  $\text{Mg}_n^+$  ion ejection from the droplet. Figure 4 shows the time-resolved PE spectra detected in covariance with  $\text{Mg}_n^+$  ( $n = 1 - 12$ ). In contrast to the transient PE spectrum of all electrons in Fig. 2, only two bands show up: A broad band ( $\alpha$ ) that extends from 0.5 to 3 eV with a slow rise and fall time, and the cross-

correlation band ( $\beta$ ) originating from three-photon ionization of gas phase Mg atoms [corresponding to band (4) in Fig. 2]. We compare covariance band ( $\alpha$ ) to the global fit results of TRPES band (2), separately in the spectral domain (Fig. 4c) and in the temporal domain (Fig. 4b). This comparison reveals good agreement in both domains, which is a strong indicator that both observables reflect the same underlying photoinduced process, especially under consideration of the difference of the experimental methods. The fact that only band (2) of the TRPES is apparent in the covariance spectrum, while band (1) is missing, shows that only the photoexcitation process represented by band (2) leads to ejection of  $\text{Mg}^+$  ions. In contrast to the dilute aggregate, photoexcitation of compact  $\text{Mg}_n$  cluster ( $\text{DAS}_1$ ) leads to immediate promotion of electrons into the detection window for one-photon ionization of the probe pulse [band (1) in Fig. 2]. Fragmentation caused by energy conversion to nuclear motion appears much less pronounced for the compact cluster so that ion ejection from the droplet is prevented, eliminating band (1) from the covariance spectrum (Fig. 4). This finding further supports our hypothetical assignment that the two bands correspond to different species with different photoexcitation dynamics: compact  $\text{Mg}_n$  cluster associated with  $\text{DAS}_1$  and the foam-like configuration associated with  $\text{DAS}_2$  and covariance band ( $\alpha$ ).

An assignment of the electron signal shown in Fig. 4 to specific cluster sizes provides additional insight into the fragmentation process. To this end, Fig. 5 shows time-integrated (0.1 - 5 ps) electron spectra correlated to the ion complexes  $\text{Mg}_{2,3}^+\text{He}_m$ ,  $\text{Mg}_{4,5}^+\text{He}_m$  and  $\text{Mg}_{6,7,8}^+\text{He}_m$ , with  $m = 0 - 5$ . The most likely energy, marked by vertical lines in Fig. 5, decreases from 2.2 eV for  $\text{Mg}_{2,3}^+\text{He}_m$  to 1.5 eV for  $\text{Mg}_{6,7,8}^+\text{He}_m$ . This development shows that electronic relaxation to energetically lower states yields smaller fragments, as more electronic energy is converted to nuclear kinetic energy.

## IV. DISCUSSION

The combination of global fitting analysis of PE spectra and electron-ion covariance detection provides evidence that He droplets enable the formation of two  $\text{Mg}_n$  configurations. These two configurations, represented by bands (1) and (2) in Fig. 2, show distinctively different photoexcitation responses, which is identified through the transient population of states with binding energies below 3.07 eV, corresponding to the one-photon detection window of the probe-pulse. We now discuss the energetics of the excitation processes leading to the population of these low-binding-energy states. Concerning band (1), compact  $\text{Mg}_n$  cluster have a lower ionization potential than the single Mg atoms and since calculated absorption spectra of small  $\text{Mg}_n$  cluster [55, 56] overlap with our pump photon energy, efficient pump-probe photoionization can be

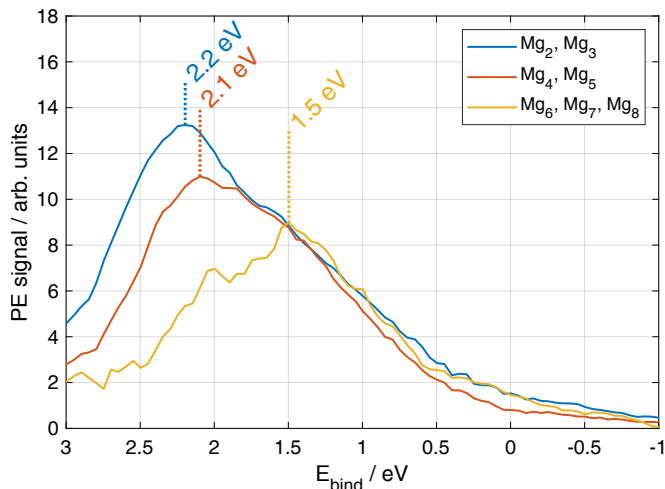


FIG. 5. Time-integrated (0.1 ps to 5 ps) photoelectron spectra correlated with different  $\text{Mg}_n^+ \text{He}_m$  ion complexes, as indicated in the legend. For the presentation, a moving mean with a width of 0.4 eV is applied.

expected (Fig. 1c). The energetics leading to band (2) are less obvious: The transition from foam-like aggregate to compact cluster is triggered by the  $3^1\text{P}_1$  atom excitation, which has a binding energy of 3.30 eV and thus lies outside the one-photon detection window. The highly excited state population of band (2) in the 0–3 eV binding energy range appears delayed, with a rise time of  $\tau_2^{\text{rise}} = (450 \pm 180)$  fs (see Fig. 2 and band ( $\alpha$ ) in Fig. 4). This raises the question about the processes leading to population of these low-binding-energy states up to the ionization continuum. A further question that will be discussed in the following is the different fragmentation behavior of the two  $\text{Mg}_n$  configurations in terms of ion ejection from the droplet.

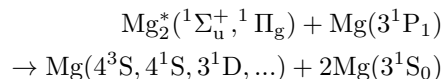
**Energy-pooling reaction.** The observed population of excited states above the pump photon energy is reminiscent of energy pooling reactions, observed in mixtures of metal vapor and a noble gas [57]. For Mg, 457.1 nm excitation of two atoms from the  $3^1\text{S}_0$  ground state to the  $3^3\text{P}_1$  excited state at 4.94 eV binding energy in a He buffer gas environment leads to population of the higher states  $3^1\text{P}_1$  and  $4^3\text{S}_1$  levels at 3.30 eV and 2.54 eV binding energy, respectively [58].

In our experiment, aggregates of cold Mg atoms are photoactivated in a dilute configuration with a Mg–Mg distance of 9.5 Å [34]. The excitation energy for the single-atom  $3^1\text{P}_1 \leftarrow 3^1\text{S}_0$  transition in this environment is slightly blue-shifted to 4.40 eV photon energy (282.5 nm), relative to the bare-atom transition at 4.35 eV (285.5 nm) [42]. The dynamics in the He solvation shell in response to the photoexcitation process [38] leads to collapse of the dilute configuration and formation of a compact  $\text{Mg}_n$  cluster. Interaction of ground-state and electronically excited Mg atoms leads to population of various states above the initially

excited  $3^1\text{P}_1$  state, as shown by the photoelectron signal in Fig. 4c. While population of these states cannot result from a two-photon excitation process (see above), energy transfer through collisions of two excited  $3^1\text{P}_1$  atoms can populate all Mg states up to the ionization potential. We thus propose a similar energy pooling reaction, based on the excited-state potential energy curves of  $\text{Mg}_2$ . [59, 60]. The reaction starts with the He-mediated formation of excited  $\text{Mg}_2^*$  molecules (see also Fig. 1c):



Collision of  $\text{Mg}_2^*$  with another excited  $\text{Mg}^*$  atom leads to population of the highly-excited states:



In the covariance spectrum shown in Fig. 4, the photoelectron band spanning from 0 to 3 eV binding energy reveals the corresponding transient population distribution. On top of Fig. 4c, electronically excited states of Mg atoms are indicated for comparison. Since  $\text{Mg}_n$  cluster up to  $n \sim 20$  atoms exhibit non-metallic van der Waals-type bonding, [61] we refer to atomic states, which are, however, not resolved in the PE spectrum due to environmental broadening and laser bandwidth. The proposed energy pooling reaction requires at least two excited Mg atoms in the foam-like aggregate. One can estimate the excitation probability of one Mg atom to be  $p_1 = 0.81 \pm 0.15$ , based on the photon absorption cross section and photon density, including experimental uncertainties (see Appendix VII C). Excitation of at least two Mg atoms is therefore quite likely.

#### Cluster formation and fragmentation dynamics.

The characteristic rise time of the transient photoelectron signal representing the highly-excited state population [ $N_2$  in Fig. 2b and band ( $\alpha$ ) in Fig. 4b] represents the transition from a foam-like Mg aggregate to a compact cluster. From parameters of the global fit population  $N_2$ , a time constant of  $\tau_2^{\text{rise}} = (450 \pm 180)$  fs for cluster formation is determined. This value agrees with the characteristic time-constant of 350 fs obtained by pump-probe strong-field ionization, which was proposed to represent the collapse of the dilute foam-like configuration [31].

Concerning nuclear dynamics, including fragmentation of the Mg aggregate and acceleration of the fragments, it is important to realize that electronic energy can be converted into kinetic energy in each step of the energy pooling reaction. Initially, He atoms carry away some of the 4.4 eV photon energy stored in  $\text{Mg}^*$  in order to form the  $\text{Mg}_2^*$  bond. In step two, the  $\text{Mg}_2^* \text{--} \text{Mg}^*$  collision can lead to the population of various higher excited  $\text{Mg}^*$  states ( $4^3\text{S}$ ,  $4^1\text{S}$ ,  $3^1\text{D}$ , ...). The difference in excitation energies of reactants (8.7 eV) and products is thus converted into Mg kinetic energy, ranging from  $\leq 3.6$  eV

for population of the  $4^3S$  state to  $\leq 1.9$  eV for population of states close to the IP (the " $\leq$ " accounts for the kinetic energy of the He atoms). [42] The released kinetic energy will increase the cluster temperature and, since the amount of energy is comparable to the binding energy of small  $Mg_n$  cluster [62], fragmentation and ejection from the droplets are expected. Figure 5 supports this assumption by showing that the population of lower electronic states is correlated with smaller clusters. This is in line with previous observations, where liberation of ions from the droplet (overcoming the solvation energy) is only possible through a release of kinetic energy [52]. Note, however, that the ionization potentials decreases with cluster size [22].

The covariance measurements also reveal that the ion-to-electron ratio decreases from 52% for gas-phase Mg atoms (a characteristic value of our covariance spectrometer) to  $\sim 15\%$  for  $Mg_n-He_N$ . This shows that the energy release is only in one out of three cases sufficient for liberation of the fragment ion from the solvation energy of the He droplet.

**Relaxation of excited cluster through electron-phonon interaction.** The decaying character of the TRPES signal in Fig. 2, observed for both compact [band (1)] and foam-like aggregates [band (2) in Fig. 2 and ( $\alpha$ ) in Fig. 4], indicate on fast electronic relaxation. The characteristic decay time constant of the compact  $Mg_n$  cluster is  $\tau_1 = (380 \pm 70)$  fs. Electronically excited metal cluster typically relax via electron-electron interaction on a time scale of less than  $\sim 100$  fs. [2, 63, 64] Our observation of a slower decay thus supports the assumption of a non-metallic complex [65], in line with recent studies showing small magnesium clusters ( $n \leq 18$ ) are not metallic [66, 67]. The electronic relaxation in van der Waals clusters proceeds through non-adiabatic transitions to lower electronic states with vibrational excitation. Electron-phonon coupling thus leads to electronically relaxed but vibrationally hot clusters.

For the  $Mg_n$  cluster formed from the foam-like configuration, the photoelectron signal decay reveals a ten times longer time constant of  $\tau_2 = (4.0 \pm 0.9)$  ps, compared to the compact cluster. This further points at the non-conductive van der Waals nature of  $Mg_n$  clusters. The significantly slower decay might be rooted in the excitation of higher electronic states due to energy pooling, or a reduced electron-to-phonon energy transfer because the formed cluster are hot and potentially reduced in size due to fragmentation. Also, cluster (fragments) ejected from the droplet loose contact to the thermal bath, keeping them vibrationally excited for longer times. The transformation of electronic to vibrational energy within  $\sim 10$  ps leads to a reduction of the cluster fragment size, as depicted in the time-resolved mass spectra in Fig. 3. Electronic relaxation of the formed cluster also manifests as increase of the  $3^1P_1$  population with a characteristic time of  $\tau_{BG}^{low} = 3.3$  ps (see band (3) in Fig. 2 and

Appendix VII B). The increasing  $3^1P_1$  population establishes agreement with the steady-state photoelectron spectra reported for dilute  $Mg_n$  ensembles in  $He_N$  [28]. In photoemission experiments using nanosecond laser pulses, a strong signal from  $3^1P_1$  and a relatively weak signal in the region above at 1–2 eV binding energy is observed. Considering that excitation and ionization occurs with two photons within a 10 ns time window, in combination with the picosecond lifetime of higher excited states and the increasing  $3^1P_1$  population, our time-domain observations are in agreement with the steady state results.

## V. CONCLUSIONS

Femtosecond time-resolved photoelectron and -ion spectroscopy and a subsequent global fitting analysis has been used to study the light-induced dynamics of small magnesium clusters with emphasis on foam-like complexes. Photoexcitation of this metastable  $Mg_n$  configuration leads to the contraction of the aggregate on a picosecond timescale. The contraction initiates the transient population of highly excited Mg states through energy pooling, as well as pronounced nuclear dynamics, which can clearly be resolved and distinguished from the compact Mg cluster response by inspecting the transient photoelectron signals.

The crucial prerequisite for this observation is the stabilization of Mg atoms at nanometer interatomic distance inside superfluid helium. First attempts to simulate these exceptional solvation properties of Mg atoms in  $He_N$  have led to contradictory results: While static DFT simulations predicted stable separation of two Mg atoms at 9.5 Å distance in He [34], path integral Monte Carlo simulations found only equilibration to strongly bound  $Mg_2$  and  $Mg_3$  molecules [37]. Clarification of this discrepancy with frequency-domain spectroscopy might be challenging because the absorption spectra of small  $Mg_n$  cluster are predicted to show a small dependence on the cluster size [55, 56], with many of them absorbing at the 4.4 eV transition of the metastable configuration [33]. Our time-domain analysis provides additional insight by revealing the photodynamical response: Photoexcitation of the foam-like  $Mg_n$  configuration triggers nuclear dynamics leading to the contraction of the aggregate. This nanometer motion of Mg atoms is represented by significantly slower transient photoelectron signals, compared to the predominantly electronic dynamics of a compact van der Waals cluster. This difference in the transient response of the two  $Mg_n$  configurations is the essential ingredient for distinguishing the overlapping spectra through global fitting analysis. Purely based on frequency-domain information, this distinctiveness is not given.

The observation that both configurations are simultaneously present within the observed  $Mg_n-He_N$  ensemble is

of relevance for cluster formation inside He droplets [25]. While the foam-like configuration is predicted to be favorable under steady-state conditions at the droplet temperature [34], this weakly-bound aggregate can collapse during the pickup phase either by a hot (insufficiently cooled) Mg atom or when the dilute aggregate exceeds a critical size [22]. Cluster aggregation inside  $\text{He}_N$ , in particular the formation of foam-like configurations, is thus governed by an interplay of kinetics and thermalization. Recent time-dependent simulations, following TD-DFT [68–71], particle-based [69, 70], or hybrid [72] approaches are able to account for such kinematic effects. These simulations reveal that the growth of compact clusters can be hindered by freezing in metastable configurations, with a certain probability depending on kinematic parameters.

Metastable separation through formation of a He barrier has been predicted, in addition to Mg [34], for rare-gas [35, 68–72] and halogen [36] atoms, as well as larger molecules [73]. Experimental evidence for the existence of a metastable configuration was reported in early deflection and mass spectrometric experiments of Ar, Kr, Xe,  $\text{H}_2\text{O}$  and  $\text{SF}_6$ , which find that the cross section for pick up is larger than that for coagulation [74]. Electronic spectroscopy of anthracene–Ar cluster in  $\text{He}_N$  revealed indications for the shielding of an attached Ar atom by a helium layer [75, 76]. Very recently, electron diffraction also found evidence for large Xe–Xe distances with He located in between [71]. In experiments with bulk liquid He, a very similar stabilization of atoms was reported [77]. Cold impurity atoms introduced into the He solvent through a supersonic jet expansion are found to condensate in an “impurity–helium solid”, characterized by a pronounced spatial separation of the impurities [78]. Such structures, investigated by means of optical spectroscopy, electron spin resonance and thermometry, were recently also observed for  $\text{H}_2\text{O}$  clusters [79, 80].

While the ability of  $\text{He}_N$  to freeze aggregates in non-equilibrium structures has long been appreciated [81], stable and well-defined large-distance separation of reactants through a solvent layer barrier provides fundamentally new perspectives for bond-formation studies. Helium droplets furthermore enable stable separation of surface-located and solvated species [29, 32] and the possibility to switch between the two locations through elec-

tronic excitation [30] or through ionization, which recently enabled the real-time observation of the primary steps of ion solvation in helium [27]. Taking into account the formation of exciplexes, consisting of excited atoms and He [82–85], shows that helium nanodroplet isolation holds great promise to study bond formation dynamics in various species. Such studies will provide insight into elementary processes accompanying the photoinduced formation of chemical bonds, such as the transient population of highly excited states above the excitation photon energy, as observed here for the formation of Mg clusters. The proposed energy pooling process relies on merging the energy of two or more excited Mg atoms to populate highly excited states. The ability of photon upconversion to trigger photoinduced processes that lie outside the available spectrum has implications in various fields, including photomedicine [86, 87]. Efficient upconversion requires close distances of the involved particles, as recently demonstrated with solid-state organic chromophore blends [88], whereas gas phase configurations suffer from prohibitory low yields due to large particle distance.[57, 58] The nanometer confinement provided by He droplets, together with flexible opportunities for generating tailor-made aggregates, provides thus a new and promising route to characterize the underlying energy and charge-transfer dynamics.

## VI. ACKNOWLEDGMENTS

We thank Wolfgang E. Ernst for useful discussions. This research was funded in whole or in part by the Austrian Science Fund (FWF) [10.55776/P33166]. For open access purposes, the authors have applied a CC BY public copyright license to any author-accepted manuscript version arising from this submission. The authors acknowledge support from NAWI Graz. MS acknowledges funding as recipient of a DOC Fellowship (26387) of the Austrian Academy of Sciences at the Institute of Experimental Physics. JT acknowledges the Deutsche Forschungsgemeinschaft (TI 210/13-1 and SFB 1477 ‘Light-Matter Interactions at Interfaces,’ Project No. 441234705) for financial support.

- 
- [1] T. Weinacht and B. J. Pearson, *Time-resolved spectroscopy an experimental perspective* (Taylor & Francis Group, 2019) p. 358.
  - [2] A. Stolow, A. E. Bragg, and D. M. Neumark, Femtosecond time-resolved photoelectron spectroscopy, *Chemical Reviews* **104**, 1719 (2004).
  - [3] I. V. Hertel and W. Radloff, Ultrafast dynamics in isolated molecules and molecular clusters, *Rep. Prog. Phys.* **69**, 1897 (2006).
  - [4] Y. Kobayashi, K. F. Chang, T. Zeng, D. M. Neumark, and S. R. Leone, Direct mapping of curve-crossing dynamics in IBr by attosecond transient absorption spectroscopy, *Science* **365**, 79 (2019).
  - [5] Y. Arasaki, K. Takatsuka, K. Wang, and V. McKoy, Pump-probe photoionization study of the passage and bifurcation of a quantum wave packet across an avoided crossing, *Physical Review Letters* **90**, 248303 (2003).
  - [6] A. Mokhtari, P. Cong, J. L. Herek, and A. H. Zewail, Direct femtosecond mapping of trajectories in a chemical



- reaction, *Nature* **348**, 225 (1990).
- [7] A. D. G. Nunn, R. S. Minns, R. Spesyvtsev, M. J. Bearpark, M. A. Robb, and H. H. Fielding, Ultrafast dynamics through conical intersections and intramolecular vibrational energy redistribution in styrene, *Physical Chemistry Chemical Physics* **12**, 15751 (2010).
- [8] M. Koch, B. Thaler, P. Heim, and W. E. Ernst, The role of rydberg–valence coupling in the ultrafast relaxation dynamics of acetone, *The Journal of Physical Chemistry A* **121**, 6398 (2017).
- [9] A. Fioretti, D. Comparat, A. Crubellier, O. Dulieu, F. Masnou-Seeuws, and P. Pillet, Formation of cold  $\text{Cs}_2$  molecules through photoassociation, *Physical Review Letters* **80**, 4402 (1998).
- [10] K. M. Jones, E. Tiesinga, P. D. Lett, and P. S. Julienne, Ultracold photoassociation spectroscopy: long-range molecules and atomic scattering, *Reviews of Modern Physics* **78**, 483 (2006).
- [11] N. V. Vitanov, T. Halfmann, B. W. Shore, and K. Bergmann, Laser-induced population transfer by adiabatic passage techniques, *Annual Review of Physical Chemistry* **52**, 763 (2001).
- [12] U. Marvet and M. Dantus, Femtosecond photoassociation spectroscopy: coherent bond formation, *Chemical Physics Letters* **245**, 393 (1995).
- [13] L. Rybak, S. Amaran, L. Levin, M. Tomza, R. Moszynski, R. Kosloff, C. P. Koch, and Z. Amitay, Generating molecular rovibrational coherence by two-photon femtosecond photoassociation of thermally hot atoms, *Physical Review Letters* **107**, 273001 (2011).
- [14] L. Rybak, Z. Amitay, S. Amaran, R. Kosloff, M. Tomza, R. Moszynski, and C. P. Koch, Femtosecond coherent control of thermal photoassociation of magnesium atoms, *Faraday Discussions* **153**, 383 (2011).
- [15] N. F. Scherer, L. R. Khundkar, R. B. Bernstein, and A. H. Zewail, Real-time picosecond clocking of the collision complex in a bimolecular reaction: the birth of OH from  $\text{H} + \text{CO}_2$ , *The Journal of Chemical Physics* **87**, 1451 (1987).
- [16] M. Gruebele, I. R. Sims, E. D. Potter, and A. H. Zewail, Femtosecond probing of bimolecular reactions: the collision complex, *The Journal of Chemical Physics* **95**, 7763 (1991).
- [17] E. D. Potter, J. L. Herek, S. Pedersen, Q. Liu, and A. H. Zewail, Femtosecond laser control of a chemical reaction, *Nature* **355**, 66 (1992).
- [18] V. Stert, P. Farmanara, H.-H. Ritze, W. Radloff, K. Gasmı, and A. Gonzalez-Urena, Femtosecond time-resolved electron spectroscopy of the intracuster reaction in  $\text{baFCH}_3$ , *Chemical Physics Letters* **337**, 299 (2001).
- [19] R. Wester, A. E. Bragg, A. V. Davis, and D. M. Neuemark, Time-resolved study of the symmetric  $\text{S}_n2$ -reaction  $\text{I}^- + \text{CH}_3\text{I}$ , *The Journal of Chemical Physics* **119**, 10032 (2003).
- [20] K. H. Kim, J. G. Kim, S. Nozawa, T. Sato, K. Y. Oang, T. W. Kim, H. Ki, J. Jo, S. Park, C. Song, T. Sato, K. Ogawa, T. Togashi, K. Tono, M. Yabashi, T. Ishikawa, J. Kim, R. Ryoo, J. Kim, H. Ihee, and S. ichi Adachi, Direct observation of bond formation in solution with femtosecond x-ray scattering, *Nature* **518**, 385 (2015).
- [21] J. H. Lee, M. Wulff, S. Bratos, J. Petersen, L. Guerin, J.-C. Leicknam, M. Cammarata, Q. Kong, J. Kim, K. B. Møller, and H. Ihee, Filming the birth of molecules and accompanying solvent rearrangement, *Journal of the American Chemical Society* **135**, 3255 (2013).
- [22] L. Kazak, K.-H. Meiwes-Broer, and J. Tiggesbäumker, Ionization potentials of  $\text{Mg}_N$  ( $N = 7\text{--}56$ ) clusters formed by spontaneous collapse of magnesium foam in helium nanodroplets, *Physical Chemistry Chemical Physics* **24**, 23350 (2022).
- [23] J. P. Toennies and A. F. Vilesov, Superfluid helium droplets: a uniquely cold nanomatrix for molecules and molecular complexes, *Angew. Chem. Int. Ed.* **43**, 2622 (2004).
- [24] C. Callegari and W. E. Ernst, Helium droplets as nanocryostats for molecular spectroscopy - from the vacuum ultraviolet to the microwave regime, in *Handbook of High Resolution Spectroscopy*, edited by F. Merkt and M. Quack (John Wiley & Sons, Chichester, 2011).
- [25] W. E. Ernst and A. W. Hauser, Metal clusters synthesized in helium droplets: structure and dynamics from experiment and theory, *Physical Chemistry Chemical Physics* **23**, 7553 (2021).
- [26] A. Slenczka and J. P. Toennies, eds., *Molecules in superfluid helium nanodroplets: spectroscopy, structure, and dynamics* (Springer International Publishing, 2022).
- [27] S. H. Albrechtsen, C. A. Schouder, A. Viñas Muñoz, J. K. Christensen, C. Engelbrecht Petersen, M. Pi, M. Barranco, and H. Stapelfeldt, Observing the primary steps of ion solvation in helium droplets, *Nature* **623**, 319 (2023).
- [28] L. Kazak, S. Göde, K.-H. Meiwes-Broer, and J. Tiggesbäumker, Photoelectron spectroscopy on magnesium ensembles in helium nanodroplets, *The Journal of Physical Chemistry A* **123**, 5951 (2019).
- [29] F. Lackner and W. E. Ernst, Photoinduced molecule formation of spatially separated atoms on helium nanodroplets, *The Journal of Physical Chemistry Letters* **9**, 3561 (2018).
- [30] A. Kautsch, M. Koch, and W. E. Ernst, Photoinduced molecular dissociation and photoinduced recombination mediated by superfluid helium nanodroplets, *Physical Chemistry Chemical Physics* **17**, 12310 (2015).
- [31] S. Göde, R. Irsig, J. Tiggesbäumker, and K.-H. Meiwes-Broer, Time-resolved studies on the collapse of magnesium atom foam in helium nanodroplets, *New Journal of Physics* **15**, 015026 (2013).
- [32] J. Poms, A. W. Hauser, and W. E. Ernst, Helium nanodroplets doped with xenon and rubidium atoms: a case study of van der waals interactions between heliophilic and heliophobic dopants, *Physical Chemistry Chemical Physics* **14**, 15158 (2012).
- [33] A. Przystawik, S. Göde, T. Döppner, J. Tiggesbäumker, and K.-H. Meiwes-Broer, Light-induced collapse of metastable magnesium complexes formed in helium nanodroplets, *Physical Review A* **78**, 10.1103/PhysRevA.78.021202 (2008).
- [34] A. Hernando, M. Barranco, R. Mayol, M. Pi, and F. Ancilotto, Density functional theory of the structure of magnesium-doped helium nanodroplets, *Physical Review B* **78**, 10.1103/physrevb.78.184515 (2008).
- [35] J. Eloranta, Self-assembly of neon into a quantum gel with crystalline structure in superfluid  $^4\text{He}$ : prediction from density functional theory, *Physical Review B* **77**, 134301 (2008).
- [36] J. Eloranta, Theoretical study of quantum gel formation in superfluid  $^4\text{He}$ , *Journal of Low Temperature Physics* **162**, 718 (2010).

- [37] E. Krotscheck and R. E. Zillich, Solvation of Mg in helium-4: Are there meta-stable Mg dimers?, *The Journal of Chemical Physics* **145**, 244317 (2016).
- [38] B. Thaler, S. Ranftl, P. Heim, S. Cesnik, L. Treiber, R. Meyer, A. W. Hauser, W. E. Ernst, and M. Koch, Femtosecond photoexcitation dynamics inside a quantum solvent, *Nat. Commun.* **9**, 4006 (2018).
- [39] L. Bruder, M. Koch, M. Mudrich, and F. Stienkemeier, Ultrafast dynamics in helium droplets, in *Molecules in Superfluid Helium Nanodroplets*, Topics in Applied Physics, edited by A. Slenczka and J. P. Toennies (Springer International Publishing, Cham, 2022) pp. 447–511.
- [40] B. Thaler, M. Meyer, P. Heim, and M. Koch, Long-lived nuclear coherences inside helium nanodroplets, *Physical Review Letters* **124**, 115301 (2020).
- [41] J. H. Nielsen, D. Pentleher, L. Christiansen, B. Shepperson, A. A. Søndergaard, A. S. Chatterley, J. D. Pickering, C. A. Schouder, A. V. Muñoz, L. Kranabetter, and H. Stapelfeldt, Laser-induced alignment of molecules in helium nanodroplets, in *Molecules in Superfluid Helium Nanodroplets*, Topics in Applied Physics, edited by A. Slenczka and J. P. Toennies (Springer International Publishing, Cham, 2022) pp. 381–445.
- [42] A. Kramida, Yu. Ralchenko, J. Reader, and NIST ASD Team, NIST Atomic Spectra Database (ver. 5.10), [Online]. Available: <https://physics.nist.gov/asd> [2023, August 11]. National Institute of Standards and Technology, Gaithersburg, MD. (2022).
- [43] M. Koch, P. Heim, B. Thaler, M. Kitzler, and W. E. Ernst, Direct observation of a photochemical activation energy: a case study of acetone photodissociation, *Journal of Physics B: Atomic, Molecular and Optical Physics* **50**, 125102 (2017).
- [44] L. J. Frasinski, K. Codling, and P. A. Hatherly, Covariance mapping: a correlation method applied to multiphoton multiple ionization, *Science* **246**, 1029 (1989).
- [45] J. Mikosch and S. Patchkovskii, Coincidence and covariance data acquisition in photoelectron and -ion spectroscopy. I. Formal theory, *Journal of Modern Optics* **60**, 1426 (2013).
- [46] J. Mikosch and S. Patchkovskii, Coincidence and covariance data acquisition in photoelectron and -ion spectroscopy. II. Analysis and applications, *Journal of Modern Optics* **60**, 1439 (2013).
- [47] I. H. van Stokkum, D. S. Larsen, and R. van Grondelle, Global and target analysis of time-resolved spectra, *Biochimica et Biophysica Acta (BBA) - Bioenergetics* **1657**, 82 (2004).
- [48] G. Wu, A. E. Boguslavskiy, O. Schalk, M. S. Schuurman, and A. Stolow, Ultrafast non-adiabatic dynamics of methyl substituted ethylenes: the  $\pi^*3s$  rydberg state, *The Journal of Chemical Physics* **135**, (2011).
- [49] D. E. Couch, H. C. Kapteyn, M. M. Murnane, and W. K. Peters, Uncovering highly-excited state mixing in acetone using ultrafast VUV pulses and coincidence imaging techniques, *The Journal of Physical Chemistry A* **121**, 2361 (2017).
- [50] P. Maierhofer, M. Bainschab, B. Thaler, P. Heim, W. E. Ernst, and M. Koch, Disentangling multi-channel photodissociation dynamics in acetone by time-resolved photoelectron-photoion coincidence spectroscopy, *J. Phys. Chem. A* **120**, 6418 (2016).
- [51] I. Wilkinson, A. E. Boguslavskiy, J. Mikosch, J. B. Bertrand, H. J. Wörner, D. M. Villeneuve, M. Spanner, S. Patchkovskii, and A. Stolow, Excited state dynamics in SO<sub>2</sub>. I. bound state relaxation studied by time-resolved photoelectron-photoion coincidence spectroscopy, *The Journal of Chemical Physics* **140**, 204301 (2014).
- [52] M. Stadlhofer, B. Thaler, and M. Koch, Dimer photofragmentation and cation ejection dynamics in helium nanodroplets, *Physical Chemistry Chemical Physics* **24**, 24727 (2022).
- [53] A. Braun and M. Drabbels, Photodissociation of alkyl iodides in helium nanodroplets. I. Kinetic energy transfer, *The Journal of Chemical Physics* **127**, 10.1063/1.2767261 (2007).
- [54] T. Döppner, T. Fennel, T. Diederich, J. Tiggesbäumker, and K. H. Meiwes-Broer, Controlling the coulomb explosion of silver clusters by femtosecond dual-pulse laser excitation, *Physical Review Letters* **94**, 013401 (2005).
- [55] I. A. Solov'yov, A. V. Solov'yov, and W. Greiner, Optical response of small magnesium clusters, *Journal of Physics B: Atomic, Molecular and Optical Physics* **37**, L137 (2004).
- [56] R. Shinde and A. Shukla, First principles electron-correlated calculations of optical absorption in magnesium clusters, *The European Physical Journal D* **71**, 301 (2017).
- [57] A. Kopystyńska and L. Moi, Energy transfer in collisions between excited atoms, *Physics Reports* **92**, 135 (1982).
- [58] D. Husain and G. Roberts, Kinetic study of Mg( $3^3P_J$ ), Mg( $3^1P_1$ ) and Mg( $4^3S_1$ ), including energy pooling, following pulsed dye-laser excitation at  $\lambda = 457.1$  nm [Mg( $3^3P_1$ )  $\leftarrow$  Mg( $3^1S_0$ )], *J. Chem. Soc., Faraday Trans. 2* **82**, 21 (1986).
- [59] S. Amaran, R. Kosloff, M. Tomza, W. Skomorowski, F. Pawłowski, R. Moszynski, L. Rybak, L. Levin, Z. Amitay, J. M. Berglund, D. M. Reich, and C. P. Koch, Femtosecond two-photon photoassociation of hot magnesium atoms: a quantum dynamical study using thermal random phase wavefunctions, *The Journal of Chemical Physics* **139**, 164124 (2013).
- [60] H. Knöckel, S. Rühmann, and E. Tiemann, The  $A^1\Sigma_u^+$  system of Mg<sub>2</sub>, *The European Physical Journal D* **68**, 293 (2014).
- [61] T. Diederich, T. Döppner, T. Fennel, J. Tiggesbäumker, and K.-H. Meiwes-Broer, Shell structure of magnesium and other divalent metal clusters, *Physical Review A* **72**, 023203 (2005).
- [62] J. Jellinek and P. H. Acioli, Magnesium clusters: structural and electronic properties and the size-induced nonmetal-to-metal transition, *The Journal of Physical Chemistry A* **106**, 10919 (2002).
- [63] A. Schirato, M. Maiuri, G. Cerullo, and G. Della Valle, Ultrafast hot electron dynamics in plasmonic nanostructures: experiments, modelling, design, *Nanophotonics* **12**, 1 (2023).
- [64] T. Hertel, E. Knoesel, M. Wolf, and G. Ertl, Ultrafast electron dynamics at Cu(111): response of an electron gas to optical excitation, *Physical Review Letters* **76**, 535 (1996).
- [65] R. M. Young, G. B. Griffin, O. T. Ehrler, A. Kammrath, A. E. Bragg, J. R. R. Verlet, O. Cheshnovsky, and D. M. Neumark, Charge carrier dynamics in semi-conducting mercury cluster anions, *Physica Scripta* **80**,

- 048102 (2009).
- [66] T. Diederich, T. Döppner, J. Braune, J. Tiggesbäumker, and K.-H. Meiwes-Broer, Electron delocalization in magnesium clusters grown in supercold helium droplets, *Physical Review Letters* **86**, 4807 (2001).
- [67] O. C. Thomas, W. Zheng, S. Xu, and K. H. Bowen, Onset of metallic behavior in magnesium clusters, *Physical Review Letters* **89**, 213403 (2002).
- [68] F. Coppens, F. Ancilotto, M. Barranco, N. Halberstadt, and M. Pi, Dynamics of impurity clustering in superfluid  $^4\text{He}$  nanodroplets, *Physical Chemistry Chemical Physics* **21**, 17423 (2019).
- [69] E. García-Alfonso, M. Barranco, D. A. Bonhommeau, N. Halberstadt, M. Pi, and F. Calvo, Clustering, collision, and relaxation dynamics in pure and doped helium nanoclusters: Density- vs particle-based approaches, *The Journal of Chemical Physics* **157**, 014106 (2022).
- [70] B. Fixot, E. Louaas, and D. A. Bonhommeau, Collision of rare-gas atoms on helium nanodroplets: Theoretical evidence for an efficient coagulation of heavy rare-gas atoms, *The Journal of Chemical Physics* **161**, 044307 (2024).
- [71] M. Trejo, A. Clifford, E. G. Alfonso, N. Halberstadt, L. Xue, and W. Kong, Electron diffraction of foam-like clusters between xenon and helium in superfluid helium droplets, *The Journal of Chemical Physics* **161**, 054306 (2024).
- [72] M. Blancafort-Jorquera, A. Vilà, and M. González, Quantum-classical approach to the reaction dynamics in a superfluid helium nanodroplet. the  $\text{Ne}_2$  dimer and Ne-Ne adduct formation reaction  $\text{Ne} + \text{Ne}$ -doped nanodroplet, *Physical Chemistry Chemical Physics* **21**, 24218 (2019).
- [73] F. Calvo, E. Yurtsever, and Ö. Birer, Possible formation of metastable pah dimers upon pickup by helium droplets, *The Journal of Physical Chemistry A* **120**, 1727 (2016).
- [74] M. Lewerenz, B. Schilling, and J. P. Toennies, Successive capture and coagulation of atoms and molecules to small clusters in large liquid helium clusters, *Journal of Chemical Physics* **102**, 8191 (1995).
- [75] E.-M. Lottner and A. Slenczka, Anthracene-argon clusters generated in superfluid helium nanodroplets: new aspects on cluster formation and microsolvation, *The Journal of Physical Chemistry A* **124**, 311 (2019).
- [76] F. Calvo and E. Yurtsever, The metastable structures of anthracene-argon clusters inside helium nanodroplets, *Theoretical Chemistry Accounts* **140**, 21 (2021).
- [77] E. B. Gordon, L. P. Mezhov-Deglin, and O. F. Pugachev, Stabilization of nitrogen atoms in superfluid helium, *Letters to JETP* **19**, 103 (1974).
- [78] E. Gordon, Impurity condensation in liquid and solid helium, *Low temperature physics* **30**, 756 (2004).
- [79] V. B. Efimov, A. N. Izotov, and L. P. Mezhov-Deglin, Helium impurity nanocluster gels in superfluid helium, *Bulletin of the Russian Academy of Sciences: Physics* **77**, 48 (2013).
- [80] L. T. Mezhov-Deglin and A. M. Kokotin, Condensed water in superfluid He-II, *Journal of Experimental and Theoretical Physics Letters* **70**, 756 (1999).
- [81] K. Nauta and R. E. Miller, Nonequilibrium self-assembly of long chains of polar molecules in superfluid helium, *Science* **283**, 1895 (1999).
- [82] J. Reho, C. Callegari, J. Higgins, W. E. Ernst, K. K. Lehmann, and G. Scoles, Spin-orbit effects in the formation of the na-he excimer on the surface of he clusters, *Faraday Discussions* **108**, 161 (1997).
- [83] C. P. Schulz, P. Claas, and F. Stienkemeier, Formation of  $\text{K}^*\text{He}$  exciplexes on the surface of helium nanodroplets studied in real time, *Physical Review Letters* **87**, 153401 (2001).
- [84] G. Droppelmann, O. Bünermann, C. P. Schulz, and F. Stienkemeier, Formation times of RbHe exciplexes on the surface of superfluid versus normal fluid helium nanodroplets, *Physical Review Letters* **93**, 023402 (2004).
- [85] M. P. Ziemkiewicz, D. M. Neumark, and O. Gessner, Ultrafast electronic dynamics in helium nanodroplets, *International Reviews in Physical Chemistry* **34**, 239 (2015).
- [86] F. Bolze, S. Jenni, A. Sour, and V. Heitz, Molecular photosensitisers for two-photon photodynamic therapy, *Chemical Communications* **53**, 12857 (2017).
- [87] M. Haase and H. Schäfer, Upconverting nanoparticles, *Angewandte Chemie International Edition* **50**, 5808 (2011).
- [88] D. H. Weingarten, M. D. LaCount, J. van de Lagemaat, G. Rumbles, M. T. Lusk, and S. E. Shaheen, Experimental demonstration of photon upconversion via cooperative energy pooling, *Nature Communications* **8**, 14808 (2017).
- [89] R. C. Hilborn, Einstein coefficients, cross sections, dipole moments, and all that, *American Journal of Physics* **50**, 982 (1982).
- [90] D. E. Kelleher and L. I. Podobedova, Atomic transition probabilities of sodium and magnesium. a critical compilation, *Journal of Physical and Chemical Reference Data* **37**, 267 (2008).
- [91] B. E. A. Saleh and M. C. Teich, *Fundamentals of photonics (wiley series in pure and applied optics)* (Wiley-Interscience, 2007) p. 1177.

## VII. APPENDIX

### A. Generation and doping of He droplets

We generate He droplets by expanding high-purity He through a 5  $\mu\text{m}$  diameter nozzle at 20 bar pressure of and 11.6 K temperature. The droplet size follows a log-normal distribution with a mean number size of  $\bar{N} = 13500$  [23]. The He droplets are doped with Mg atoms inside a resistively heated oven, where the number of Mg atoms entering the droplet can be controlled by changing the metal vapor pressure via the oven heating current. A quadrupole mass spectrometer is used to monitor the Mg pickup conditions. The  $\text{Mg}_n$  aggregate size limit can be estimated from the mass-to-charge spectrum in Fig. 3, where  $\text{Mg}_8^+$  corresponds to the highest detected mass-to-charge ratio. By assuming that the parent cluster was split in half during pump-probe ionization, the largest initial cluster size can be estimated with  $\text{Mg}_{16}$ . To characterize the influence of the Mg doping level on bands (1)–(3) in the photoelectron spectrum (Fig. 2), the corresponding photoelectron signals are shown in Fig. 6 as a function of the Mg oven heating current. While band (1) (2 to 3 eV binding energy) increases steadily with rising oven current, band (2) (0.5 to 2 eV binding energy) shows a local maximum at around 28 A. This opposing signal dependency for large doping levels supports the assignment of band (1) to compact  $\text{Mg}_n$  clusters and band (2) to a foam-like  $\text{Mg}_n$  configuration and is in line with the recent observation of spontaneous foam collapse for higher Mg doping levels [22]. PE band (3), associated with single Mg atoms (-0.5 to 0.5 eV binding energy) is most prevalent at lower oven currents, and is strongly suppressed for larger oven currents, confirming that the He droplets contain multiple Mg atoms for the applied heating current of 29 A.

### B. Global fitting

For our global fitting analysis, the following two types of transient decay functions are used: (i) An instantaneously rising signal followed by exponential decay is modelled by a decay function of the form

$$N_i(t) = \frac{1}{2} e^{\frac{\sigma^2}{2\tau_i^2} - \frac{(t-t_0)}{\tau_i}} \operatorname{erfc}\left(-\frac{t-t_0}{\sqrt{2}\sigma} + \frac{\sigma}{\sqrt{2}\tau_i}\right), \quad (1)$$

which is obtained through convolution of a Gaussian function with a full halfwidth  $\sigma$  (representing the temporal instrument response function) centered at time zero,  $t_0$ , and a single exponential decay function with characteristic decay time  $\tau_i$  [47]. In Eq. 1  $\operatorname{erfc}(z) = 1 - \operatorname{erf}(z)$ .

(ii) Modeling of a delayed signal rise followed by an exponential decay is achieved through a sequential model, in which state A is excited by the pump pulse and decays with time constant  $\tau_A$  into state B, which itself sub-

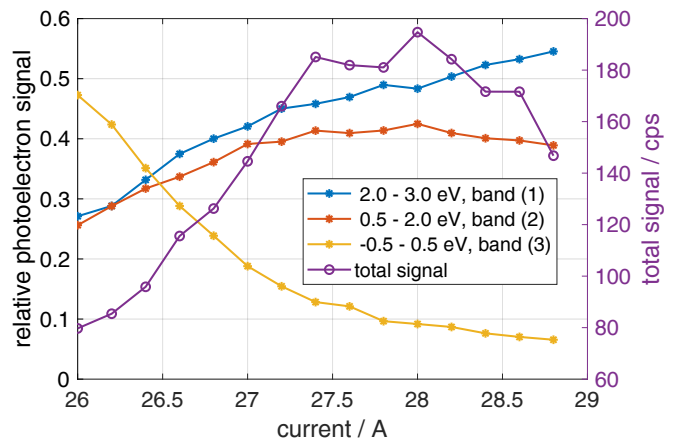


FIG. 6. Dependence of the pump-probe photoelectron bands (c.f., Fig. 2) on the Mg doping level, represented as heating current applied to the Mg pickup oven. The photoelectron spectra for different heating currents are normalized and the depicted photoelectron signal is obtained through integration within the energy intervals given in the legend, and in time from -1 ps to 11 ps.

sequentially decays with time constant  $\tau_B$ . The corresponding decay function reads

$$N_i(t) = [N_A(t, \tau_A) - N_B(t, \tau_B)] \frac{\tau_A}{2(\tau_A - \tau_B)}, \quad (2)$$

where  $N_A(t, \tau_A)$  and  $N_B(t, \tau_B)$  are represented by Eq. 1. The time constant  $\tau_A$  thus corresponds to the characteristic rise time of the population  $N_i(t)$ , labeled  $\tau_i^{\text{rise}}$  in the main text, whereas  $\tau_B$  corresponds to the characteristic decay time of  $N_i(t)$ , labeled  $\tau_i$ . In addition to the three DAS and corresponding decay functions discussed in the main text, in both energy regions an exponentially increasing background is considered by using Eq. 2 with a corresponding rise time and a very long decay time of 1  $\mu\text{s}$ . The fitting procedure reveals that the background in the low binding energy region has a rise time of  $\tau_{BG}^{\text{low}} = (3300 \pm 1200)$  fs and in the higher binding energy region has a rise time of  $\tau_{BG}^{\text{high}} = (200 \pm 1200)$  fs. There is still some interplay between DAS<sub>3</sub> and crosscorrelation in the low binding energy region, which suggests that  $N_3$  might rise slightly slower than the single decay fit function allows with the temporal instrument response of  $\sigma = 170$  fs. However, switching to a two-level decay fit function does not improve the fit for band (3). Figure 7a summarizes all decay functions, and the corresponding decay associated spectra are shown in Fig. 7b. In Fig. 8 the quality of the fit result can be evaluated by comparing the measured time-resolved photoelectron spectrum in (a) to the global fit model in (b). The residuals in (c) show that the deviation between the two is below 10 % throughout the majority of the spectrum.

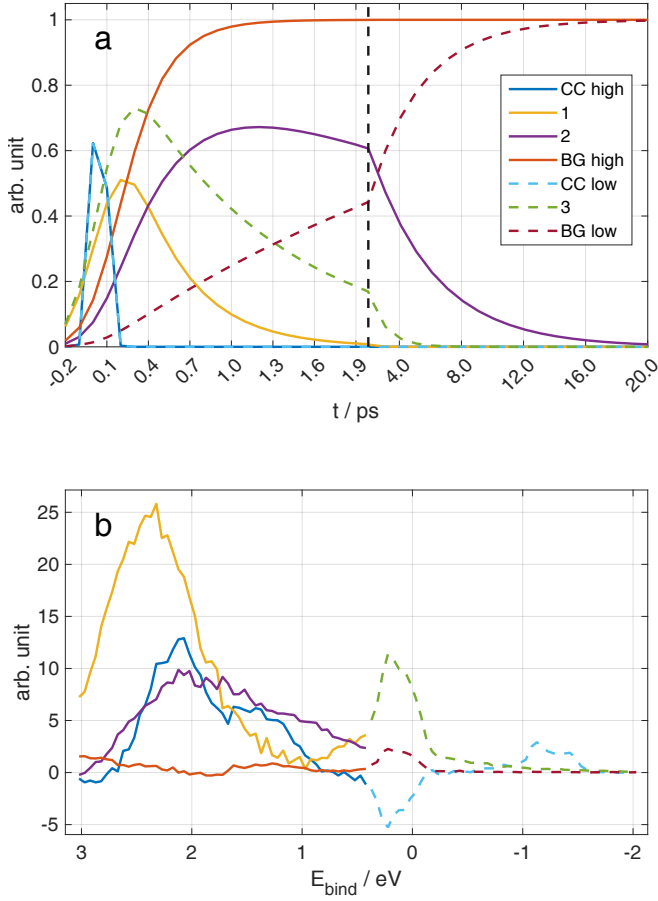


FIG. 7. Overview of the global fit analysis. **(a)** Time-dependent decay functions for each decay associated spectrum. Note that the time-scale changes at 2 ps, indicated with the black-dashed vertical line. The crosscorrelation functions are abbreviated as CC, and the background functions as BG. Background and crosscorrelation also have the identifier high and low, which refers to the low or high binding energy region (see main text). **(b)** Decay associated spectra corresponding to the decay functions in (a).

### C. Excitation probability for Mg atoms inside helium droplets

The energy pooling process outlined in the main text requires at least two excited Mg atoms inside a droplet. We therefore estimate the excitation probability of the Mg atoms for the applied laser parameters. The probability  $p_{\text{abs}}$  of a single photon from the pump laser pulse to be absorbed by one Mg atom is given by the ratio of absorption cross section  $\sigma_{\text{abs}}$  and the laser beam area  $A$ :

$$p_{\text{abs}} = \frac{\sigma_{\text{abs}}}{A} \quad (3)$$

#### Calculation of the absorption cross section $\sigma_{\text{abs}}$

Since the width of the absorption spectrum of Mg atoms solvated inside He droplets [33] is comparable to the

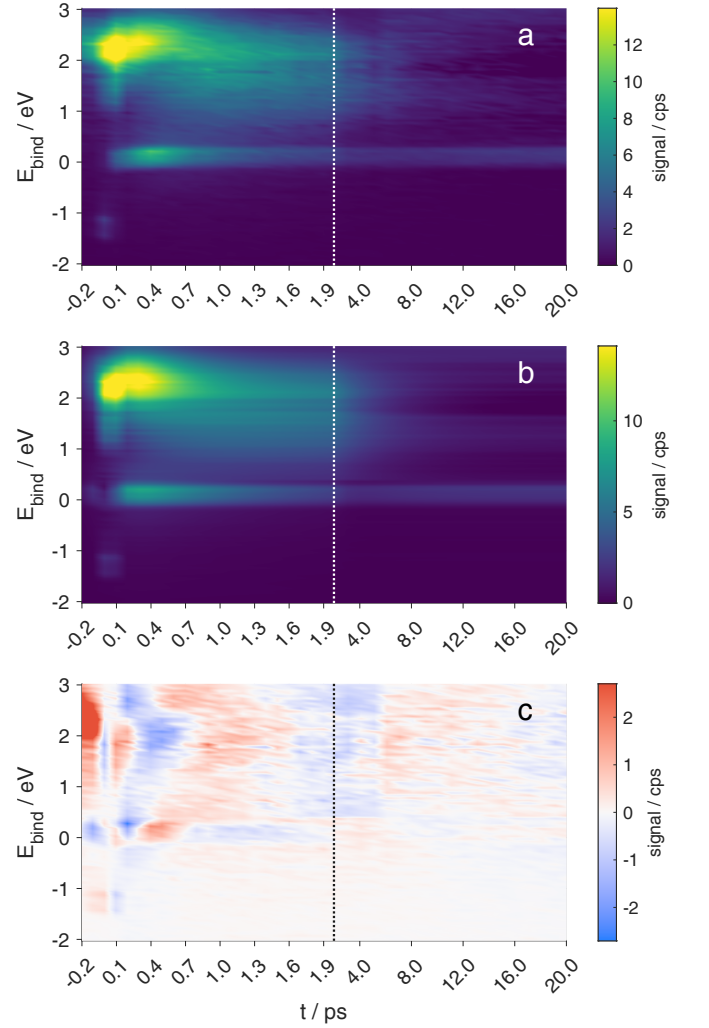


FIG. 8. Evaluation of the global fit model. **(a)** Measured time-resolved photoelectron spectrum as depicted in Fig. 2a **(b)** Reconstruction of the time-resolved photoelectron spectrum, obtained by summing up all DAS contributions. **(c)** Residual plot obtained as difference of the measured (a) and reconstructed (b) spectra.

spectral width of the short laser pulses, the absorption cross section  $\sigma_{\text{abs}}$  can be calculated by multiplying the frequency-integrated absorption cross section  $\sigma_0$  with the overlap integral  $I_{\text{overlap}}$  of the line shape function of the broadened atom transition  $g(\omega)$  and the spectral line shape of the laser pulse  $\rho(\omega)$ :

$$\sigma_{\text{abs}} = \sigma_0 \times I_{\text{overlap}} = \sigma_0 \int_{-\infty}^{\infty} g(\omega)\rho(\omega)d\omega \quad (4)$$

Note that  $g(\omega)$  and  $\rho(\omega)$  are in units of s/rad. The frequency-integrated absorption cross section  $\sigma_0$  for the Mg atom transition  $3^1P_1 \leftarrow 3^1S_0$  follows from the Einstein  $A_{21}$  coefficient [89]:

$$\sigma_0 = \frac{1}{4} \frac{g_2}{g_1} \lambda^2 A_{21}$$

Here  $g_2 = 3$  and  $g_1 = 1$  are the degeneracies in the upper and lower level, respectively, and  $\lambda$  is the excitation wavelength. With the Einstein spontaneous emission rate for Mg of [90]

$$A_{21} = 4.91 \times 10^8 \text{s}^{-1}$$

and the  $3^1P_1 \leftarrow 3^1S_0$  transition wavelength of Mg atoms in He droplets of [33]

$$\lambda = 282.5 \text{ nm},$$

we obtain the frequency-integrated absorption cross section  $\sigma_0$  of

$$\sigma_0 = 2.90389 \times 10^{-5} \text{ m}^2 \frac{\text{rad}}{\text{s}}$$

In using this value, we are assuming that the spontaneous emission rate for Mg does not change when the atoms are inside the helium droplet i.e. that the broadened lineshape is not caused by a shorter lifetime of the excited state.

For the spectral line shape of the laser pulse  $\rho(\omega)$ , a Gaussian spectrum with standard deviation  $s_{\text{laser}}$  centered at the mean angular frequency  $\omega_0$  is assumed:

$$\rho(\omega) = \frac{1}{\sqrt{2\pi}s_{\text{laser}}} e^{-(\omega-\omega_0)^2/(2s_{\text{laser}}^2)}$$

From the measured spectrum of the pump pulses, with a full width at half maximum (FWHM) bandwidth of  $\Delta\rho = 3.5 \text{ nm}$  centered at  $282.5 \text{ nm}$ , the standard deviation of the laser spectrum in units of angular frequency can be calculated:

$$s_{\text{laser}} = 3.51 \times 10^{13} \text{ rad/s}$$

For the absorption spectrum of Mg in helium droplets, we also assume a Gaussian line shape with a FWHM of  $\Delta g = 4 \text{ nm}$ , [33] yielding a standard deviation of the line shape function of

$$s_{\text{abs}} = 4.01 \times 10^{13} \text{ rad/s}.$$

With the spectral distributions of the laser and absorption line, we can calculate the overlap integral:

$$I_{\text{overlap}} = 7.488 \times 10^{-15} \text{ s/rad}$$

The final cross section according to Eq. (4) is then

$$\sigma_{\text{abs}} = 2200 \text{ Mb}.$$

### Calculation of the laser beam area.

For a Gaussian beam, the area  $A(z)$  and diameter  $d(z)$  as function of the distance  $z$  to the beam waist are given by the following relations [91]:

$$A(z) = \pi \left( \frac{d(z)}{2} \right)^2$$

TABLE II. Laser beam parameters:  $E_{\text{pulse}}$  ... pulse energy,  $D$  ... diameter of the laser beam at the lens,  $z$  ... distance to the beam waist,  $f$  ... focal length of the lens,  $M^2$  ... beam quality factor.

$E_{\text{pulse}} / \mu\text{J}$	$D / \text{mm}$	$z / \text{mm}$	$f / \text{mm}$	$M^2$
1	2	0	1000	1.35

$$d(z) = d_0 \sqrt{1 + \left( \frac{z}{z_R} \right)^2}$$

$$z_R = \frac{\pi d_0^2}{4\lambda}$$

$$d_0 = \frac{4\lambda f M^2}{\pi D},$$

where  $f$  is the focal length of the lens,  $\lambda$  is the laser wavelength,  $M^2$  is the beam quality and  $D$  is the diameter of the laser beam at the lens. With the laser beam parameters listed in Tab. II, we obtain the following value for the laser focus area:

$$A = 4.63 \times 10^{14} \text{ Mb}$$

### Calculation of the excitation probability.

The single photon absorption probability of a Mg atom inside a He droplet, calculated according to Eq. (3), is:

$$p_{\text{abs}} = \frac{2.2 \times 10^3 \text{ Mb}}{4.63 \times 10^{14} \text{ Mb}} = 4.75 \times 10^{-12}$$

For the  $N$  photons contained in a laser pulse, the excitation process can be modeled by a Bernoulli trial, i.e., the probability that at least one photon excites the atom follows a Bernoulli distribution:

$$p_1 = \sum_{n=0}^{N-1} p_{\text{abs}} \times (1 - p_{\text{abs}})^n = 1 - (1 - p_{\text{abs}})^N \quad (5)$$

The number of photons  $N$  in the pulse can be calculated from the pulse energy  $E_{\text{pulse}}$  and photon energy ( $\hbar\omega_0$  neglecting the bandwidth of the laser):

$$N = \frac{E_{\text{pulse}}}{\hbar\omega_0}$$

For the value of  $p_{\text{abs}} = 4.75 \times 10^{-12}$ , pulse energy of  $1 \mu\text{J}$  and photon energy of  $h \times 1.061 \cdot 10^{15} \text{ Hz}$ , Eq. (5) yields a pump-pulse excitation probability of a single Mg atom inside a He droplet of

$$p_1 = 0.9988.$$

Since this value is derived for optimal laser beam parameters, which might deviate in the experiment, we assume

TABLE III. Mean and standard deviation for the parameters used in random sampling:  $E_{\text{pulse}}$  . . . pulse energy,  $D$  . . . laser beam diameter at the focusing lens,  $z$  . . . sample position with respect to the laser beam waist.

	$E_{\text{pulse}} / \mu\text{J}$	$D / \text{mm}$	$z / \text{mm}$
mean	1.0	2.0	0
standard deviation	0.2	0.5	50

a Gaussian distribution of the parameters  $E_{\text{pulse}}$ ,  $D$  and  $z$  (see Tab. III) and apply statistical sampling to generate a distribution for the excitation probability, from which we determine the mean and standard deviation. Large uncertainties of the parameters are chosen in order to obtain a robust estimate for the excitation probability. For each set of random sample parameters, an excitation probability  $p_1$  is calculated. In Fig. 9, the pulse energy  $E_{\text{pulse}}$  and laser beam diameter  $d$  (at the sample) are chosen to depict the dependency of the excitation probability in a 2D plot, together with the contour lines of the  $p_1(d, E_{\text{pulse}})$  function.

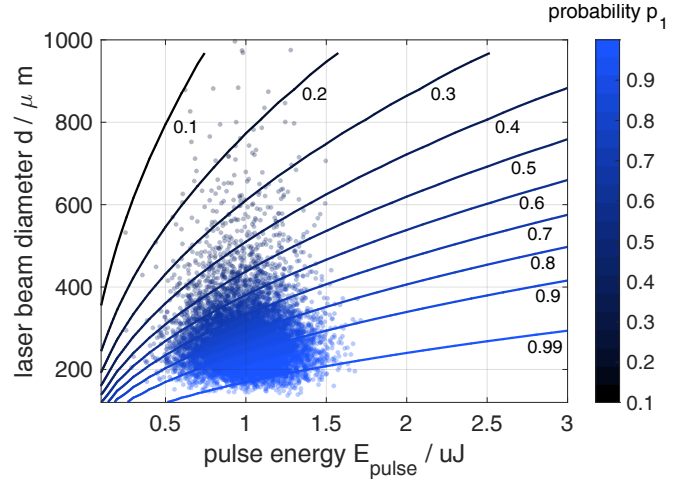


FIG. 9. Sampled probabilities  $p_1$ , for one Mg atom to be excited by  $N$  photons. The contours and colors are used to indicate the excitation probability for a given laser beam diameter  $d$  and pulse energy  $E_{\text{pulse}}$ .

Fig. 10 shows a histogram of the sampled probabilities  $p_1$ , which can be interpreted as a probability density for the excitation probability  $p_1$ , resulting from the distributions of input parameters. The numerical mean and standard deviation of this distribution are  $p_1 = 0.81$  and  $\sigma_{p_1} = 0.15$ , showing that Mg atom excitation inside He droplets is very likely for a broad range of experimental laser parameters. The high single-atom excitation probability makes excitation of multiple atoms inside a single droplet plausible.

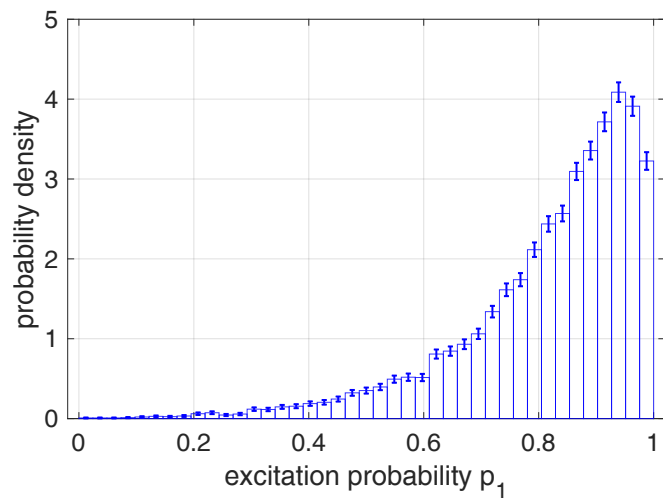


FIG. 10. Numerical probability density for the excitation probability  $p_1$ , given the uncertainty in pulse energy, beam diameter at the lens and distance from sample in Table III.